

Article

Effect of Nickel Oxide Doping to Ceria-Supported Gold Catalyst for CO Oxidation and Water-Gas Shift Reactions

Miao Shu ^{1,4}, Shuai Wei ², Chun-Jiang Jia ², Dao-Lei Wang ³ and Rui Si ^{1,*}

¹ Shanghai Synchrotron Radiation Facility, Shanghai Institute of Applied Physics, Chinese Academy of Sciences, Shanghai 201204, China; shumiao@sinap.ac.cn

² Key Laboratory for Colloid and Interface Chemistry, Key Laboratory of Special Aggregated Materials, School of Chemistry and Chemical Engineering, Shandong University, Jinan 250100, China; weishuai@mail.sdu.edu.cn (S.W.); jiacj@sdu.edu.cn (C.-J.J.)

³ Division of China, TILON Group Technology Limited, Shanghai 200090, China; gavin.wang@tilon.com.cn

⁴ University of Chinese Academy of Science, Beijing 100049, China

* Correspondence: sirui@sinap.ac.cn; Tel.: +86-3393-2079

Received: 31 August 2018; Accepted: 27 September 2018; Published: 26 November 2018



Abstract: Ceria-supported gold catalyst has drew much research interest owing to its high reactivity on CO oxidation and water-gas shift (WGS) reactions. However, till now, there were relatively limited studies on the effect of secondary metal/metal oxide component into gold-ceria system to enhance its catalytic performance. In this work, we synthesized the ceria supported gold-nickel samples via a deposition-precipitation method with the base of NaHCO₃ to adjust final pH value of 8~9. We found that the addition of nickel oxide drove off the gold species from the stock solution during synthesis, and thus resulted in a dramatical decrease on doped Au concentration. No crystallized phases of gold and nickel were observed on the surface of ceria nanorods in both X-ray diffraction (XRD) and transmission electron microscopy (TEM). The valence of nickel was maintained as Ni²⁺ for all the measured samples by X-ray photoelectron spectroscopy (XPS), while gold was oxidized with the increased nickel amount after analysis of X-ray absorption near edge spectroscopy (XANES). The corresponding catalytic tests showed that with the introduction of nickel oxide, the activity of gold-ceria catalyst was promoted for the WGS reaction, but inhibited for the CO oxidation reaction.

Keywords: gold; ceria; nickel oxide; CO oxidation; water-gas shift

1. Introduction

There are considerable research have ascertained that supported metal catalysts, especially to gold catalysts, are extraordinarily active for oxidation of carbon monoxide ($2\text{CO} + \text{O}_2 = 2\text{CO}_2$) [1–6] and water-gas shift ($\text{CO} + \text{H}_2\text{O} = \text{CO}_2 + \text{H}_2$) [7–12] reaction. Up to present, a great deal of research work has focused on the “structure-activity” relationship in supported gold catalyst, such as the type of oxide support [1,7,13–17], the gold size effect [17–20], the oxidation state of gold [21] and the metal-support interaction [5,17]. For instance, Carretin et al. reported that nanocrystalline CeO₂ supported gold nanoparticles are more active than those anchored on other oxides (TiO₂, Fe₂O₃) for CO oxidation [1]. Si et al. synthesized CeO₂ to produce three shapes (nanorod, nanocube, nanopolyhedron) as the support, and the light-off profiles of WGS reaction elucidated that rod-like CeO₂ expose more {110} and {100} planes which are most active for gold stabilization and activation [7]. Fu et al. confirmed that gold nanoparticles are essential for some oxidation reactions, but unimportant in WGS reaction over Au-ceria [22]. On the basis of these findings, we can see the significant importance of physical and chemical properties of Au modified by the matrix.

Although single metal gold catalyst has been studied profoundly during the last two decades, the research on the bimetallic gold catalyst was still limited [23–25], especially for the effect of low-price transition metal or metal oxide doping [24,26,27]. Few practical preparation routes have been achieved in the fine control on the formation of bimetallic catalyst at the subnanometer scale [26,27]. For example, Scott et al. reported the synthesis and characterization of TiO₂-supported Pd-Au bimetallic nanoparticle catalysts prepared using dendrimer-encapsulated nanoparticles [23] and Eveline et al. prepared Pt-Au bimetallic cluster supported on the SiO₂ or TiO₂ by wet impregnation to investigate the electronic structure of platinum and gold differed from that in the monometallic clusters [25]. However, the size of bimetallic cluster or nanoparticle were larger than 2 nm in the above work. On the other hand, it is extremely difficult to precisely explore the electronic structure and geometric structure of low-concentration active metals. In recent years, combination between aberration-corrected transmission electron microscopy (TEM) and X-ray adsorption fine structure (XAFS) techniques provide a comprehensive characteristic approach to identify the structural information on small-size bimetallic species anchored on the surface of oxide matrix [11,28–30]. Previously, Qiao et al. took the lead in proposing the single atom catalyst that FeO_x supported Pt single-atom and characterized by aberration-corrected high-angle annular dark-field scanning transmission electron microscopy (HAADF-STEM) and XAFS, revealed that Pt isolated single atoms structure [28], Guo et al. compared different Au species (atom, cluster, particle) and confirmed the metal gold is the active species during CO oxidation with the help of HAADF-STEM and XAFS techniques [21]. These investigations confirmed the possibility of obtaining reliable and accurate structural information around gold active species.

Owing to the easily reversible transformation between Ce³⁺ and Ce⁴⁺, nanosized cerium oxide (CeO₂) always applied to the reducible oxide support to deposit different metals or oxide [1,22]. For example, our group prepared conformably dispersed subnanometer copper [31] and iron [32] oxide clusters on CeO₂. Our previous findings also indicated that ceria-supported gold catalyst is very active for both CO oxidation [21] and WGS [7] reactions. In addition, some research groups found the synergetic effect of gold and nickel [33,34]. For example, Shirakawa et al. reported the gold atoms improve the release of oxygen from nickel atoms of NiO within cluster [33]. Thus, in this work, we tried to combine the effect of nickel on gold activity and the structure-activity relationship on WGS and CO oxidation reactions. Herein, in this work, we report the synthesis of nanorod-like ceria-supported gold-nickel catalyst via a deposition-precipitation method with bicarbonate sodium as precipitating agent, as well as the multiple characterizations such as X-ray diffraction (XRD), X-ray photoelectron spectroscopy (XPS), TEM and XAFS towards the comprehensive structural properties of these nickel-doped gold-ceria samples. Furthermore, we elucidate the effect of nickel oxide in catalysis by catalytic tests for both CO oxidation and WGS reactions, in which the introduction of nickel displays totally different performance (positive/negative effect) on the above reactions.

2. Results

2.1. Effect of Nickel Oxide during Deposition of Gold

In this work, the concentration of gold or nickel was designed to be fixed at 1 or 5 at%, respectively. During the catalyst preparation, we investigated three different precipitating agents: ammonium carbonate ((NH₄)₂CO₃), sodium carbonate (Na₂CO₃) and sodium hydrogen carbonate (NaHCO₃), and found that: (1) (NH₄)₂CO₃ is very suitable for gold deposition onto pure ceria [7], but nickel ion was complexed with molecular ammonia, which is prejudicial to the deposition of nickel; (2) When Na₂CO₃ is added, the fast growth of nickel phase made the NiO crystallized easily; (3) If NaHCO₃ is used as precipitant, no large-size gold or nickel phase appeared. Therefore, we finally selected sodium hydrogen carbonate as the base to simultaneously precipitate both gold and nickel ions.

Table 1 shows that the experimental loading of gold concentrations (Au), determined by inductively coupled plasma atomic emission spectroscopy (ICP-AES), are 0.21 and 0.13 at% for

ceria-supported pure gold (AuCe) and gold-nickel (AuNiCe) samples, respectively. Clearly, there was ca. 40% loss of gold species during the applied deposition-precipitation process. Here, we hypothesized that the as-formed Ni(OH)_x(H₂O)_y nucleation in stock solution can cover part of ceria surface and drive the Au(OH)_x(H₂O)_y nuclei off from the oxide support. Since the purpose of this work is focused on the formation of small-size gold and nickel atoms or clusters, we accepted this gold loss, which could be compensated by the normalization of catalytic reactivity.

Table 1. Au and Ni bulk concentration, atomic ratios (Ni/(Ni + Ce)) on the surface, BET Specific surface areas (S_{BET}), BJH (Barett-Joyner-Halenda) pore volume (V_p), lattice constants (a) of CeO₂, averaged grain sizes (D) for AuNi/CeO₂ samples.

Sample	Au (at%) ^a	Ni (at%) ^a	S_{BET} (m ² /g) ^c	V_p (cm ³ /g) ^c	a (Å) ^d	D_{XRD} (nm) ^d	D_{TEM} (nm) ^g
AuCe	0.21(0.04)	-	99	0.44	5.4134(2) 5.4157(3) ^e 5.4100(1) ^f	9.4	8.1(1.8) ^h 20–150 ⁱ
AuNiCe	0.13(0.05)	3.9(0.1) 4.5, 3.8, 4.3 ^b	99	0.53	5.4088(1) 5.4108(1) ^e 5.4149(1) ^f	9.7	8.7(1.9) ^h 20–150 ⁱ

^a Determined by ICP-AES; ^b Determined by XPS for fresh, used after CO oxidation and used after WGS, respectively; ^c From N₂ adsorption/ desorption; ^d From XRD; ^e After CO oxidation reaction; ^f After WGS reaction; ^g From TEM; ^h Width; ⁱ Length. Numbers in brackets are errors.

2.2. Structural and Textural Properties for Ceria-Supported Gold-Nickel Catalysts

The nitrogen adsorption/desorption experiment was used to investigate the textural properties for fresh samples. Table 1 shows that BET specific surface areas of AuCe and AuNiCe identical (99 m²/g). The related adsorption/desorption isotherms and pore diameter distribution histograms are shown in Figure 1a,b, respectively. All the adsorption/desorption curves are defined as the type IV isotherm. The hysteresis loop appear in the P/P^0 range of 0.8–1.0 associated with AuCe or AuNiCe is type H3, which identifies the materials consisted of aggregated particles [35]. Figure 1b shows that AuNiCe appears slightly larger average pore diameter (20.5 nm)/BJH pore volumes (0.53 cm³/g) than those for AuCe (18.3 nm, 0.44 cm³/g), indicating the addition of nickel may add extra surface layers of ceria nanorods. Nevertheless, all the above data demonstrate that the introduction of Ni actually did not bring major changes for the textural properties of our ceria-supported gold catalyst.

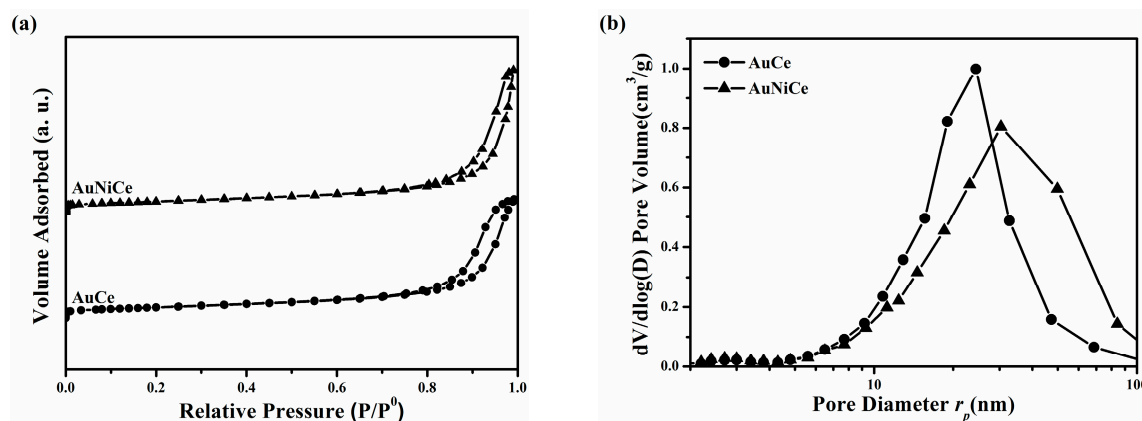


Figure 1. N₂ adsorption measurements of fresh AuNi/CeO₂ samples: (a) adsorption-desorption isotherm; (b) BJH pore size distribution.

TEM and high resolution transmission microscopy (HRTEM) were used to verify the morphology of ceria supported gold-nickel samples. As shown in Figure 2, CeO₂ support is composed by nanorods

with 20–150 nm length and uniform diameter, and their average widths (8.1–8.7 nm) are nearly the same between **AuCe** and **AuNiCe** (see Table 1). Figure 3a,c confirm the *fcc* structure for CeO₂ in both of the investigated samples, and no lattice fringes of Au or Ni/NiO were detected. Figure 3b,d verify the homogenous dispersions of either Au or Ni on the surface of CeO₂ for both pure and Ni-doped Au/CeO₂ catalysts at the nanometer scale by the aids of scan transmission electron microscopy-energy dispersive spectrometer (STEM-EDS) mappings. Thus, on the basis of microdomain characterizations, we can draw a conclusion that the introduced gold and nickel ions were uniformly converted to deposited species on the surface of CeO₂ nanorods during our synthesis.

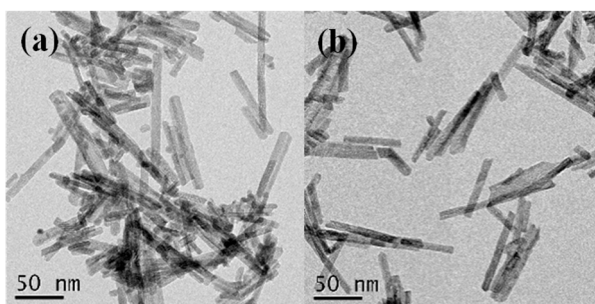


Figure 2. TEM images of fresh AuNi/CeO₂ samples: (a) AuCe; (b) AuNiCe.

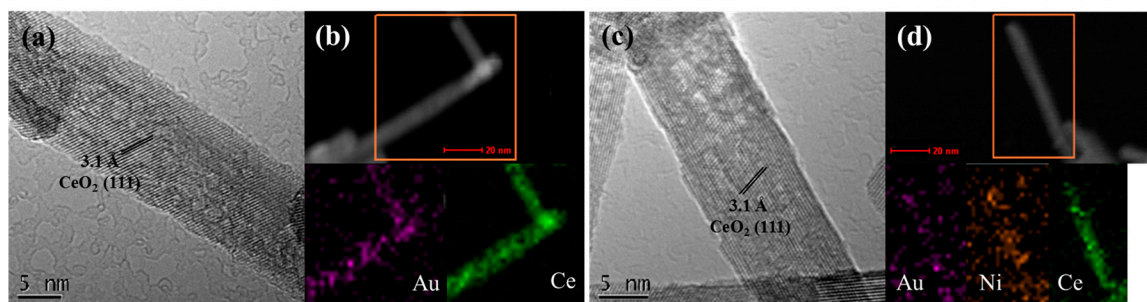


Figure 3. HRTEM images (a,c) and STEM-EDS mapping results (b,d) of fresh AuNi/CeO₂ samples: (a,b) AuCe; (c,d) AuNiCe.

2.3. Catalytic Performance of Ceria-Supported Gold-Nickel Catalysts

The catalytic performance of the as-synthesized ceria supported gold-nickel samples was evaluated by both CO oxidation and WGS reactions. Figure 4a,b display the limited activity of gold-free samples (**NiCe**) for these two reaction, confirming the importance of Au to activate the CO conversion. Figure 4a shows that the introduction of nickel impaired the reactivity of gold-ceria catalyst. Correspondently, Table 2 lists that the temperature of 50% conversion (T_{50}) for CO oxidation is raised from 50 °C (**AuCe**) to 66 °C (**AuNiCe**), and the reaction rate normalized by gold amount at 40 °C decreases from 1030 (**AuCe**) to 631 $\mu\text{mol g}_{\text{Au}}^{-1} \text{s}^{-1}$ (**AuNiCe**). The higher reaction rate obtained over gold-ceria samples is comparable to that of Au supported on ceria nanorods synthesized by deposition-precipitation with NaOH as precipitating agent under the same reaction conditions (1167 $\mu\text{mol g}_{\text{Au}}^{-1} \text{s}^{-1}$) [15]. On the other hand, Figure 4b shows the activity in WGS reaction as a function of reaction temperature. Clearly, the addition of nickel significantly promoted the reactivity of gold-ceria catalyst. It is important to highlight that the reaction rate normalized by gold concentration at 250 °C increases from **AuCe** (781 $\mu\text{mol g}_{\text{Au}}^{-1} \text{s}^{-1}$) to **AuNiCe** (2542 $\mu\text{mol g}_{\text{Au}}^{-1} \text{s}^{-1}$, see Table 2). Therefore, we can draw a conclusion that the nickel doping indeed has positive effect for the WGS reaction, while negative effect for the CO oxidation reaction in this work.

Table 2. H₂ reduction temperatures (T_R); H₂ theoretical and real consumption values; temperatures of 50% conversion (T_{50}) and reaction rates (r) of CO oxidation and WGS reactions for AuNi/CeO₂ samples.

Sample	T_R (°C) ^a	H ₂ Consump. (μmol/g _{cat})	T_{50} (°C) CO Oxidation ^c	r (μmol g _{Au} ⁻¹ s ⁻¹)	
				CO Oxidation ^c (40 °C)	WGS ^d (250 °C)
AuCe	118	341 ^a (5) ^b	50	1030	781
AuNiCe	146	1278 (525)	66	631	2542

^a Calculate from H₂-TPR (5% H₂/Ar, 30mL/min); ^b Calculate from Au^{δ+} → Au⁰ and Ni²⁺ → Ni⁰; ^c Test in CO oxidation reaction (1% CO/20% O₂/79% N₂); ^d Test in WGS reaction (2% CO/10% H₂O/88% N₂). Consump.: Consumption.

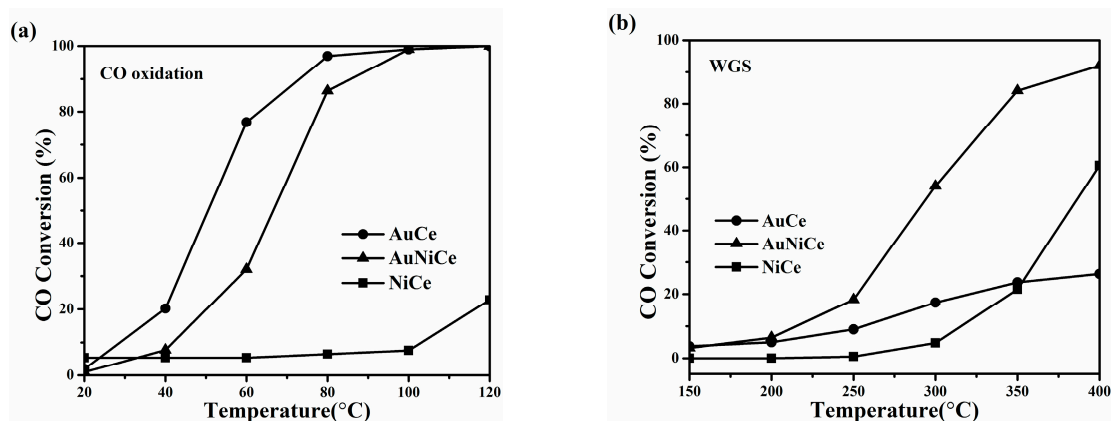


Figure 4. “Light off” profiles of AuNi/CeO₂ samples for: (a) CO oxidation reaction (1% CO/20% O₂/79% N₂, 80,000 mL g_{cat}⁻¹ h⁻¹); (b) WGS reaction (2% CO/10% H₂O/88% N₂, 84,000 mL g_{cat}⁻¹ h⁻¹).

2.4. Structural and Textural Properties for Used Ceria-Supported Gold-Nickel Catalysts

To better understand the origin of doping effect by nickel over the studied gold-ceria catalyst, we further investigated the related samples by the aids of more characterization techniques. Figure 5 shows that fresh AuCe and AuNiCe are of *fcc* CeO₂ phase (JCPDS card no.: 34-394) with lattice constants a around 5.41 Å and the average grain size of 9.4–9.7 nm (see Table 1). Beyond that, there is no other component including Au or Ni/NiO can be identified in the patterns, which is in good agreement with the TEM results. It is probably due to the low loading of Au and/or small-size atoms or clusters of deposited Au or Ni species over the ceria surface.

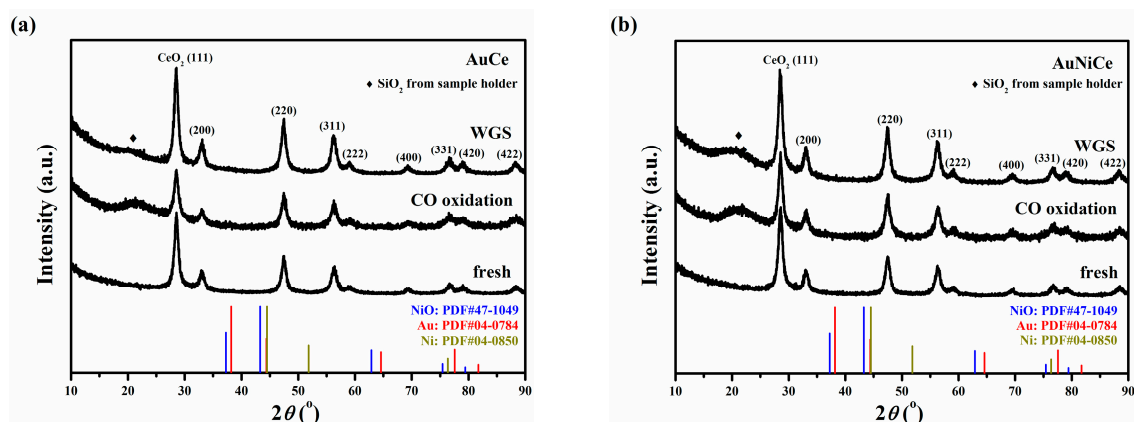


Figure 5. XRD patterns of AuNi/CeO₂ samples before and after different reactions: (a) AuCe; (b) AuNiCe.

Crystal structures of ceria supported gold-nickel samples after both CO oxidation and WGS reactions were also determined by XRD. Figure 5 exhibit that the all the measured catalysts maintained the pure *fcc* ceria phase as that of fresh catalyst. Still, no patterns of Au or Ni/NiO were detected and the lattice constants (*a*) of used catalysts are similar to those of fresh (see Table 1), revealing the relatively stable gold and nickel species during these two reactions [36,37] and/or low contents of gold and nickel.

The HRTEM images of used Au/CeO₂ and AuNi/CeO₂ samples in Figure 6a,c,e,g determine the presence of *fcc* CeO₂ phase in both **AuCe** and **AuNiCe** after either CO oxidation or WGS reactions. The corresponding STEM-EDS mapping results in Figure 6d,f,h verify the well dispersion of gold after reaction for the tested AuNi/CeO₂ catalysts, except that ~5 nm Au nanoparticles appeared for **AuCe** after CO oxidation (Figure 6b), indicating the agglomeration of small-size gold species under CO + O₂ working conditions without the addition of nickel.

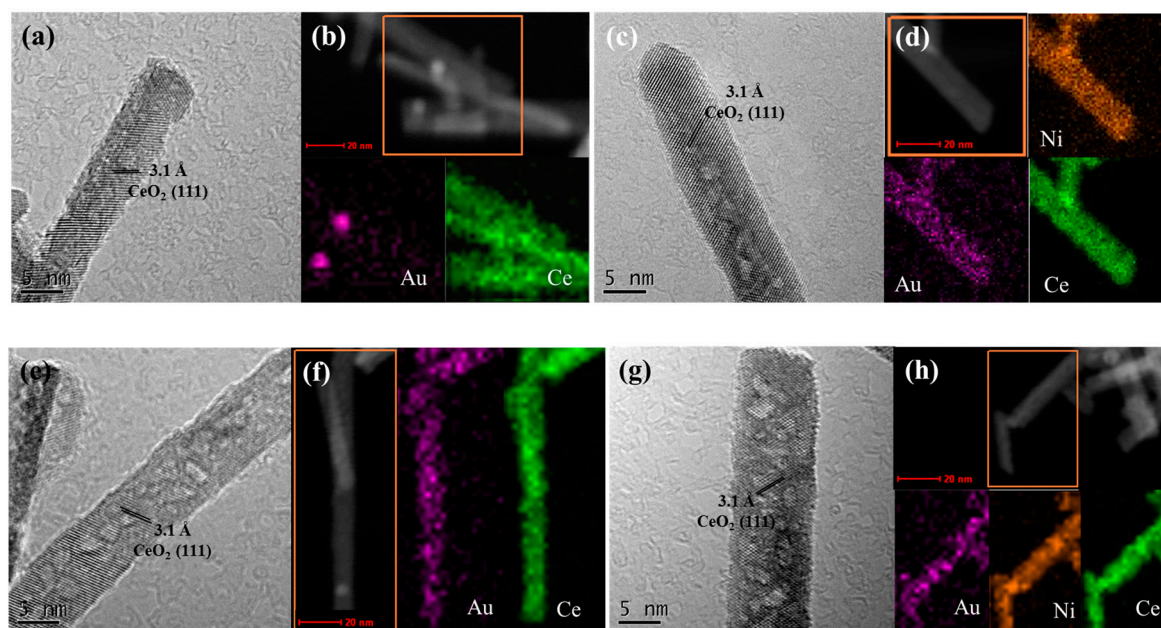


Figure 6. HRTEM images (a,c,e,g) and STEM-EDS mapping results (b,d,f,h) of used AuNi/CeO₂ samples after CO oxidation (a–d) and WGS (e–h) reactions: (a,b,e,f) **AuCe**; (c,d,g,h) **AuNiCe**.

2.5. Electronic Structure of Gold and Nickel for Ceria-Supported Catalysts

X-ray absorption near edge structure (XANES) spectroscopy was carried out to determine the electronic structure of Au in this work. Seen in Figure 7a,b, the oxidation of gold was totally different between **AuCe** and **AuNiCe**. We have run linear combination fits, and obtained the average valence states of gold to be +0.3 and +1.7 for fresh **AuCe** (Figure 7c) and **AuNiCe** (Figure 7d), respectively. Clearly, with the addition of secondary metal (Ni), the oxidized gold species become dominant on the ceria surface. Figure 7 also depicts the totally different XANES profiles of Au L3 edge for used catalysts from those of fresh samples. The intensity of white-line of **AuCe** sample slightly oxidized after CO oxidation reaction, but obviously decreased after WGS reaction (Figure 7a). For the **AuNiCe** sample, the intensity of white-line drastically decreased after both CO oxidation and WGS reactions (Figure 7b). It is worthwhile mentioning that the Au still obtained oxidized after CO oxidation, but almost equal to pure Au foil (Au⁰) after WGS reaction [38,39], whatever nickel is doped or not. It reveals that the reaction conditions of CO + H₂O significantly reduce more fraction of gold species supported on the ceria surface than those of CO + O₂.

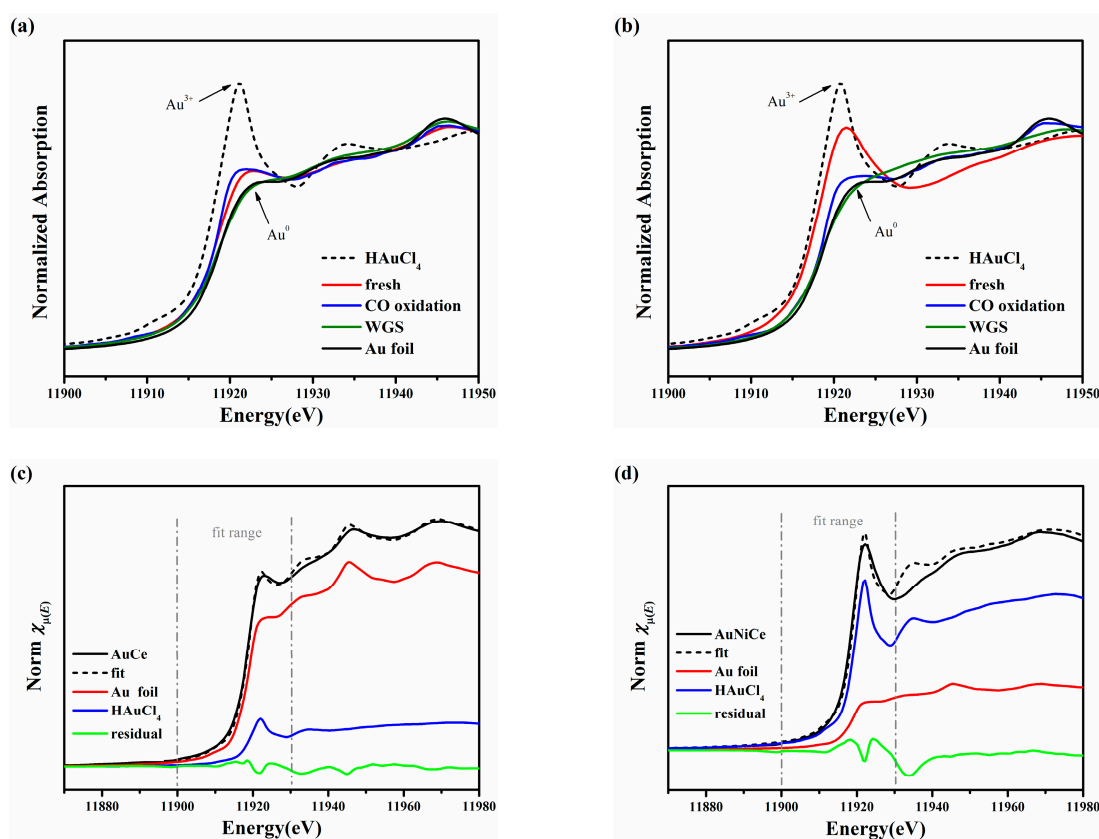


Figure 7. XANES profiles of AuNi/CeO₂ samples before and after different reactions: (a) AuCe; (b) AuNiCe; (c) linear combination fit on fresh AuCe; (d) linear combination fit on fresh AuNiCe.

Owing to the influence of intensive fluorescence of Ce, the Ni edge cannot be measured by XAFS. Here, we applied X-ray photoelectron spectroscopy (XPS) to verify the electronic structure of nickel. Figure 8a exhibits that the unique Ni²⁺ species for the nickel-containing samples, whether before or after the catalytic tests. Table 1 displays that the surface concentration of nickel (fresh: 4.5 at%; used in CO oxidation: 3.8 at%; used in WGS: 4.3 at%) is almost identical the bulk concentration of nickel (3.9 at%), manifesting no nickel segregation on the surface of ceria nanorods. Besides, Figure 8a exhibits that the valence of nickel for all the used samples was remained as Ni²⁺ after either CO oxidation or WGS reaction. Thus, the nickel species did not change their electronic structure during reaction. In another word, the state of gold is more important to the catalytic reactivity of our AuNi/CeO₂ samples.

The temperature-programmed reduction by hydrogen (H₂-TPR) was performed to investigate the reducibility and metal-support interaction for the ceria-supported gold-nickel catalysts. Figure 8b exhibits that no observable reduction was found for pure ceria nanorods, and the peaks at 184 and 257 °C for NiCe can be assigned to the reduction of surface oxygen species of CeO₂ and Ni^{δ+} species interacting with the CeO₂ [36,40]. A broad reduction bands at 118 °C for the AuCe, which can be attributed to the Au^{δ+} species interacting with CeO₂ [7]. Remarkably, the reduction peaks for the AuCe was maintained but shifted to higher temperature after the addition of nickel (Figure 8b and Table 2), possibly due to the stronger interaction between nickel-modified gold and ceria support [36]. Similarly, the reduction temperatures for nickel-containing species were also much lower in AuNiCe than the gold-free NiCe sample, revealing the interaction between gold and nickel oxide to form Au-O-Ni structure. The H₂ consumption values of all the tested samples are listed in Table 2. It must be mentioned that the real consumption of H₂ in experiment is significantly higher than those theoretical (only considering Au^{δ+} → Au⁰ and Ni²⁺ → Ni⁰). This could be explained by the partial reduction of ceria support (Ce⁴⁺ → Ce³⁺) starting around 100 °C, which is activated by either gold or nickel oxide

species. On the basis of the above H₂-TPR results, we can identify the interactions of both metal to support and gold to nickel in our study.

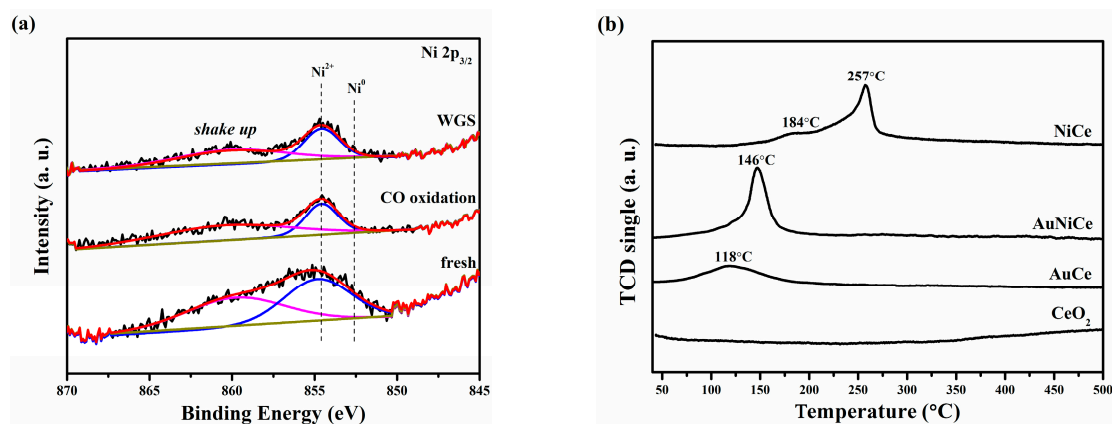


Figure 8. (a) XPS spectra of Ni 2p for AuNiCe; (b) H₂-TPR profiles for fresh AuNi/CeO₂ samples.

3. Discussion

3.1. Effect of Nickel Oxide to Gold-Ceria Catalyst for CO Oxidation Reaction

It is generally accepted that Ni deposited on the CeO₂ has supremely low even hardly any activity for CO oxidation reaction between 20 and 120 °C [37,40,41], and we also observed the same results during the catalytic tests (NiCe, Figure 4a). Hence, the reactivity of investigated catalysts in this work should be correlated to the structural and textural properties of gold itself. Previously, Deng et. al reported the metallic Au⁰ species favor the CO oxidation reaction in Au-Ce-O and Au-Fe-O systems, which was demonstrated by the comparison between different states (oxidation pretreatment and reduction pretreatment) for the catalytic measurements [14]. In our study, we found the distinct structural changes of gold when nickel was introduced, and thus the two samples (AuCe and AuNiCe) show obvious differences in activity for CO oxidation process. Combining the XANES results on gold, we confirmed that the fraction of metallic Au decreased, as well as the activity of samples decreased with the addition of nickel, which is in a good agreement with the argument that metallic gold is active species for CO oxidation [21]. Here, we emphasized the importance of comparison on normalized reaction rate (*r*) by gold amount to exclude the variation on the Au concentration in each sample (Table 2). In one word, metallic gold is indeed active for the low-temperature CO oxidation reaction.

3.2. Effect of Nickel Oxide to Gold-Ceria Catalyst for Water-Gas Shift Reaction

On the other hand, for the investigated WGS reaction, we found a totally contrast phenomenon towards the CO oxidation reaction. First, NiCe has catalytic reactivity for this reaction, but very limited below 300 °C (Figure 4b). We have determined a clear conclusion on the order of WGS activity: AuNiCe > AuCe > NiCe (Figure 4b), especially for the low-temperature (up to 300 °C) reaction. Here, according to our XANES data (Figure 7b), the ionic gold species, which was promoted by the addition of nickel component, benefit the catalytic performance of ceria supported catalysts for the WGS reaction. Analogously, Fu et al. removed the gold particles with NaCN aqueous solution leaching and remained very fine clusters or atomically dispersed gold which were identified as ionic Au, and such gold species were proved to be very important to WGS reaction [22]. Later on, considerable researchers have been devoted to the cationic gold are the active species [7,22]. In this work, we designed another approach and prepared two samples with totally different oxidation state of Au by the addition of nickel, and compared the activity of ceria-supported gold catalysts with after the normalization by gold amount. Finally, we disclosed that the normalized reaction rate increased with the decreased fraction of ionic gold in Au-Ni-Ce-O system (Table 2). However, the XANES results on used samples indicate the reduction of ionic Au^{δ+} species during the WGS reaction, especially for

AuNiCe (Figure 7b). It indicates that the ionic gold species were converted to dominantly metallic Au during WGS. However, the initial small-size $\text{Au}^{\delta+}$ species interacting with either nickel oxide (Au-O-Ni) or ceria support (Au-O-Ce) effectively kept the active gold atoms/clusters survived after the catalytic measurement, and thus held the high reactivity on WGS, which is well consistent with our previous findings demonstrated by in-situ XAFS results [42].

In this work, there was no special treatment between the end of catalytic tests and the structural characterization of XANES on gold. Since the as-formed metallic Au^0 component from ionic $\text{Au}^{\delta+}$ species under WGS reaction conditions is not easy to be reoxidized by air in room temperature (actually 400 °C was required revealed by in-situ XAFS and cyclic H_2 -TPR) previously [42], we believe the used catalysts after these two reactions (considering the reducing potential in CO oxidation is much lower than that in WGS) should largely maintained their structural evolution completed during the catalytic tests.

4. Materials and Methods

4.1. Raw Materials

All the reagents used in this work were purchased from Sinopharm Chemical Reagent Co., all of which were analytical grade and without purified any more.

4.2. Preparation of Ceria Nanorods

The CeO_2 nanorods synthesized by hydrothermal approach [13]. $\text{Ce}(\text{NO}_3)_3 \cdot 6\text{H}_2\text{O}$ (0.05 mol/L) was added into NaOH (6 mol/L) solution (70 mL) with vigorous stirring about 15 min. The suspension was moved into Teflon bottle (inner volume: 100 mL) and then tightly seal in stainless-steel autoclave. Hydrothermal treatment operated at 100 °C for 24 h. Then, the precipitates were washed by Millipore (>18 M Ω) water (ca. 1000 mL) four times and alcohol (ca. 250 mL) once. The as-washed ceria nanorods were dried in vacuum under 70 °C for 12 h.

4.3. Preparation of Gold-Nickel Cluster on Ceria

Ceria supported gold-nickel catalyst were synthesized according to deposition-precipitation (DP) method. The atomic percentage of gold was designed to be 1 at%, the nickel was adjusted to be 5 at%. The NaHCO_3 (8.4 g) and calcined ceria nanorods (1 g) were stirred in 180 mL Millipore (>18 M Ω) water to form a buffering solution with pH value of ~9. $\text{HAuCl}_4 \cdot 4\text{H}_2\text{O}$ and $\text{Ni}(\text{NO}_3)_2 \cdot 6\text{H}_2\text{O}$ were dissolved in 20 mL Millipore water and then slowly dropped into the above stock solution, and still aged at room temperature for 1 h. The precipitates were separated by centrifugation and washed by Millipore water for three times. The as-washed powders were dried in vacuum at 65 °C for 12 h and further calcined in air at 400 °C for 4 h (heating rate: 2 °C/min). The prepared ceria-supported gold-nickel clusters were denoted as **AuCe** and **AuNiCe** for single metal and bimetallic samples, respectively.

4.4. Characterizations

The experimental concentration of gold and nickel were detected by inductively coupled plasma atomic emission spectroscopy (ICP-AES) with IRIS Intrepid II XSP instrument (Thermo Electron Co., Waltham, MA, USA).

The nitrogen adsorption-desorption characterizations were analyzed on an ASAP2020-HD88 analyzer (Micromeritics Co., Ltd., Atlanta, GA, USA) at 77 K. The as-calcined powders were degassed at 250 °C under vacuum (<100 mm Hg) over 4 h before the introduction of N_2 . The pore size (r_p) distribution of each sample was calculated on the basis of desorption branch of the tested isotherms with the BJH method. The BET specific surface areas (S_{BET}) were counted from data between 0.05 and 0.20 in the relative pressure.

The powder X-ray diffraction (XRD) patterns were experimented on Bruker D8 Advance diffractometer (Bruker Co., Billerica, MA, USA) (40 kV, 40 mA) using Cu $K\alpha_1$ radiation ($\lambda = 1.5406 \text{ \AA}$),

with a scanning rate of $4^\circ/\text{min}$. The 2θ angles were calibrated with a μm -scale alumina ($\alpha\text{-Al}_2\text{O}_3$) standard. The diffraction patterns of samples were gathered from 10 to 90° with $0.02^\circ/\text{step}$. The ground sample was planished on a quartz sample holder before each test. Cell dimensions of cubic CeO_2 were obtained from the corresponding powder data with the “LAPOD” software of least-squares refinement by Cohen’s method [43,44].

The transmission electron microscopy (TEM), high-resolution transmission electron microscopy (HRTEM) images and scanning transmission electron microscopy-energy dispersive spectrometer (STEM-EDS) elemental mapping results were obtained from a FEI Tecnai G2 F20 microscope (FEI Co., Hillsboro, TX, USA) executing at 200 kV, equipped with a Genesis XM2 accessory (EDAX Inc., Mahwah, NJ, USA). Samples were ultrasonic dispersed in absolute alcohol about 5 min, and then placed a drop of liquid supernatant on an ultra-thin (3–5 nm) carbon film-coated Cu grid. The sample grid was dried spontaneously under dark conditions before inserted into the sample holder.

The X-ray photoelectron spectroscopy (XPS) measurements were performed on an Axis Ultra XPS spectrometer (Kratos Co., Manchester, UK) of Al $K\alpha$ radiation (225 W). The binding energies were calibrated by C 1s line at 284.8 eV.

4.5. X ray Absorption Fine Structure

The X-ray absorption fine structure (XAFS) spectroscopy at the Au L3 ($E_0 = 11919$ eV) edge was operated at 3.5 GeV in “top-up” mode with a constant current of 260 mA at the BL14W1 beamline [45] of the Shanghai Synchrotron Radiation Facility (SSRF). The XAFS data were collected with a 7-element Ge solid state detector in fluorescence mode. The X-ray energy was calibrated with the absorption edge of pure Au foil. Before the XAFS measurement, we ground the investigated sample into fine powders (smaller than 200 mesh), and then pressed the pure sample without any dilution to a solid pellet.

The profiles of X-ray absorption near edge structure (XANES) part were pretreated and fitted with Athena software. The “normalized absorption” was defined as experimental absorption coefficients as a function of energies $\mu(E)$ were processed by background subtraction and normalization procedures. The chemical valence of Au was determined with the linear combination fit [46] by comparison to the corresponding references of Au foil and HAuCl_4 based on the normalized XANES profiles in Athena software.

4.6. Catalytic Tests

The reducibility of samples were probed with temperature-programmed reduction by hydrogen (H_2 -TPR) operated in a Builder PCA-1200 instrument (BJBUILDER Optics Co., Ltd., Beijing, China), and the consumption of hydrogenation determined with a thermal conductivity detector (TCD) (BJBUILDER Optics Co., Ltd., Beijing, China). The 30 mg laminar and sieved samples (40–60 mesh) were initially oxidized in pure O_2 at 300°C for 30 min and cooled naturally to room temperature before reduction. The reduction process was performed with a gas mixture of 5 vol.% H_2/Ar (Jinan Deyang Co., Jinan, China, 99.997% purity) from room temperature to 500°C (flowing rate: 30 mL/min; heating rate: $5^\circ\text{C}/\text{min}$).

The catalytic test for CO oxidation reaction over ceria-supported gold-nickel samples were estimated in a plug flow reactor, in which the thermocouple is placed on the top of the samples and connected with a PID controller (YUDIAN Co., Xiamen, China). The variations of CO and CO_2 in outlets were monitored by a non-dispersive Gasboard 3500 IR spectroscopy (Wuhan Sifang Co., Wuhan, China). The 50 mg of sieved (40–60 mesh) samples were pretreated in air at 300°C for 30 min before test and cooled down to room temperature in pure N_2 . Then, a gas mixture of 1 vol.% CO/20 vol.% O_2/N_2 (99.997% purity, Jinan Deyang Co., Jinan, China) passed through the catalysts at a flow rate of 67 mL/min, corresponding to a space velocity of $80,000\text{ mL}\cdot\text{h}^{-1}\text{ g}_{\text{cat}}^{-1}$. The “light off” profiles were obtained with the changes of CO conversions from 20 to 150°C with a ramping rate of $3^\circ\text{C}/\text{min}$. The whole measurement of CO oxidation reaction took ca. 43 min. The CO conversion was calculated with the following equations: $\text{CO conversion (\%)} = (\text{CO}_{in} - \text{CO}_{out})/\text{CO}_{in} \times 100$. In the kinetic experiments,

the reaction rates were calculated on the basis of data points of less than 20% CO conversions to exclude the mass transfer limitation.

The catalytic test of water gas shift (WGS) reaction activities were evaluated in the plug flow reactor, and the thermocouple was placed on the top of the catalysts and connected with a PID controller. All outlet gases were monitored by a Gasboard 3500 IR spectroscopy (Wuhan Sifang Co., Wuhan, China). 50 mg of sieved (40–60 mesh) sample was pretreated with 5% H₂/Ar gas mixture at 300 °C for 30 min. The reactant gas consisting of 2 vol.% CO/N₂ (99.997% purity, Jinan Deyang Co., Jinan, China) was fed to mix with water vapor (CO:H₂O = 1:5) at a flow rate of 70 cm³/min with a total GHSV of 84,000 cm³ g⁻¹ h⁻¹. The reactant temperature began from 150 °C to 400 °C under the heating rate 5 °C/min and the catalytic data were recorded at 50 °C per step. The whole measurement of WGS reaction took 7–8 h. The CO conversion of WGS is calculated according to the following equation: CO conversion (%) = (CO_{in} – CO_{out})/CO_{in} × 100. In the kinetic experiments, the reaction rates were calculated on the basis of data points of less than 20% CO conversions to exclude the mass transfer limitation.

5. Conclusions

In this work, gold-ceria catalysts doped with nickel were synthesized by the deposition-precipitation method. The use of NaHCO₃ as precipitating agent drove part of the gold species off from the ceria surface. The corresponding catalytic tests demonstrated that the addition of nickel shows positive effect to the WGS reaction, while negative effect to the CO oxidation reaction. On the basis of multiple characterization means including XRD, XPS, XANES and TEM/HRTEM, we verified that the ionic gold may benefit WGS process and the metallic gold may promote the reactivity of gold-ceria catalyst for the CO oxidation reaction. Furthermore, the main contribution of nickel oxide is to tune the electronic structure of active gold species.

Author Contributions: R.S. conceived and designed the experiments; M.S. performed the experiments and analyzed the data; S.W. and D.-L.W. contributed part of catalytic measurements; M.S., R.S. and C.-J.J. wrote the paper.

Funding: Financial supported from the National Science Foundation of China (NSFC) (grant nos. 21773288 and 21331001), the Excellent Young Scientists Fund from NSFC (grant no. 21622106), the Outstanding Scholar Fund (grant nos. JQ201703) from the Science Foundation of Shandong Province (China), the Taishan Scholar Project of Shandong Province (China).

Conflicts of Interest: The authors declare no conflict of interest.

References

1. Carrettin, S.; Concepcion, P.; Corma, A.; Lopez Nieto, J.M.; Puentes, V.F. Nanocrystalline CeO₂ increases the activity of Au for CO oxidation by two orders of magnitude. *Angew. Chem. Int. Ed.* **2004**, *43*, 2538–2540. [[CrossRef](#)] [[PubMed](#)]
2. Herzing, A.A.; Kiely, C.J.; Carley, A.F.; Landon, P.; Hutchings, G.J. Identification of active gold nanoclusters on iron oxide supports for CO oxidation. *Science* **2008**, *321*, 1331–1335. [[CrossRef](#)] [[PubMed](#)]
3. Li, X.N.; Yuan, Z.; He, S.G. CO oxidation promoted by gold atoms supported on titanium oxide cluster anions. *J. Am. Chem. Soc.* **2014**, *136*, 3617–3623. [[CrossRef](#)] [[PubMed](#)]
4. Li, Z.Y.; Yuan, Z.; Li, X.N.; Zhao, Y.X.; He, S.G. CO oxidation catalyzed by single gold atoms supported on aluminum oxide clusters. *J. Am. Chem. Soc.* **2014**, *136*, 14307–14313. [[CrossRef](#)] [[PubMed](#)]
5. Guo, Y.; Gu, D.; Jin, Z.; Du, P.P.; Si, R.; Tao, J.; Xu, W.Q.; Huang, Y.Y.; Senanayake, S.; Song, Q.S.; et al. Uniform 2 nm gold nanoparticles supported on iron oxides as active catalysts for CO oxidation reaction: Structure-activity relationship. *Nanoscale* **2015**, *7*, 4920–4928. [[CrossRef](#)] [[PubMed](#)]
6. Centeno, M.; Ramírez Reina, T.; Ivanova, S.; Laguna, O.; Odriozola, J. Au/CeO₂ Catalysts: Structure and CO Oxidation Activity. *Catalysts* **2016**, *6*, 158. [[CrossRef](#)]
7. Si, R.; Flytzani-Stephanopoulos, M. Shape and crystal-plane effects of nanoscale ceria on the activity of Au-CeO₂ catalysts for the water-gas shift reaction. *Angew. Chem. Int. Ed.* **2008**, *47*, 2884–2887. [[CrossRef](#)] [[PubMed](#)]

8. Rim, K.T.; Eom, D.; Chan, S.W.; Flytzani-Stephanopoulos, M.; Flynn, G.W.; Wen, X.D.; Batista, E.R. Scanning tunneling microscopy and theoretical study of water adsorption on Fe₃O₄: Implications for catalysis. *J. Am. Chem. Soc.* **2012**, *134*, 18979–18985. [[CrossRef](#)] [[PubMed](#)]
9. Yang, M.; Allard, L.F.; Flytzani-Stephanopoulos, M. Atomically dispersed Au-(OH)_x species bound on titania catalyze the low-temperature water-gas shift reaction. *J. Am. Chem. Soc.* **2013**, *135*, 3768–3771. [[CrossRef](#)] [[PubMed](#)]
10. Yang, M.; Li, S.; Wang, Y.; Herron, J.A.; Xu, Y.; Allard, L.F.; Lee, S.; Huang, J.; Mavrikakis, M.; Flytzani-Stephanopoulos, M. Catalytically active Au-O(OH)_x- species stabilized by alkali ions on zeolites and mesoporous oxides. *Science* **2014**, *346*, 1498–1501. [[CrossRef](#)] [[PubMed](#)]
11. Yao, S.; Zhang, X.; Zhou, W.; Gao, R.; Xu, W.; Ye, Y.; Lin, L.; Wen, X.; Liu, P.; Chen, B.; et al. Atomic-layered Au clusters on α-MoC as catalysts for the low-temperature water-gas shift reaction. *Science* **2017**, *357*, 389–393. [[CrossRef](#)] [[PubMed](#)]
12. Flytzani-Stephanopoulos, M. Gold atoms stabilized on various supports catalyze the water-gas shift reaction. *Acc. Chem. Res.* **2014**, *47*, 783–792. [[CrossRef](#)] [[PubMed](#)]
13. Mai, H.X.; Sun, L.D.; Zhang, Y.W.; Si, R.; Feng, W.; Zhang, H.P.; Liu, H.C.; Yan, C.H. Shape-Selective Synthesis and Oxygen Storage Behavior of Ceria Nanopolyhedra, Nanorods, and Nanocubes. *J. Phys. Chem. B* **2005**, *109*, 24380–24385. [[CrossRef](#)] [[PubMed](#)]
14. Deng, W.; Carpenter, C.; Yi, N.; Flytzani-Stephanopoulos, M. Comparison of the activity of Au/CeO₂ and Au/Fe₂O₃ catalysts for the CO oxidation and the water-gas shift reactions. *Top. Catal.* **2007**, *44*, 199–208. [[CrossRef](#)]
15. Huang, X.S.; Sun, H.; Wang, L.C.; Liu, Y.M.; Fan, K.N.; Cao, Y. Morphology effects of nanoscale ceria on the activity of Au/CeO₂ catalysts for low-temperature CO oxidation. *Appl. Catal. B* **2009**, *90*, 224–232. [[CrossRef](#)]
16. Lai, S.; Qiu, Y.; Wang, S. Effects of the structure of ceria on the activity of gold/ceria catalysts for the oxidation of carbon monoxide and benzene. *J. Catal.* **2006**, *237*, 303–313. [[CrossRef](#)]
17. Shekhar, M.; Wang, J.; Lee, W.S.; Williams, W.D.; Kim, S.M.; Stach, E.A.; Miller, J.T.; Delgass, W.N.; Ribeiro, F.H. Size and support effects for the water-gas shift catalysis over gold nanoparticles supported on model Al₂O₃ and TiO₂. *J. Am. Chem. Soc.* **2012**, *134*, 4700–4708. [[CrossRef](#)] [[PubMed](#)]
18. Janssens, T.V.W.; Clausena, B.S.; Hvolbæk, B.; Falsig, H.; Christensen, C.H.; Bligaard, T.; Nørskov, J.K. Insights into the reactivity of supported Au nanoparticles: Combining theory and experiments. *Top. Catal.* **2007**, *44*, 15–26. [[CrossRef](#)]
19. Chen, S.; Luo, L.; Jiang, Z.; Huang, W. Size-Dependent Reaction Pathways of Low-Temperature CO Oxidation on Au/CeO₂ Catalysts. *ACS Catal.* **2015**, *5*, 1653–1662. [[CrossRef](#)]
20. Taketoshi, A.; Haruta, M. Size- and Structure-specificity in Catalysis by Gold Clusters. *Chem. Lett.* **2014**, *43*, 380–387. [[CrossRef](#)]
21. Guo, L.W.; Du, P.P.; Fu, X.P.; Ma, C.; Zeng, J.; Si, R.; Huang, Y.Y.; Jia, C.J.; Zhang, Y.W.; Yan, C.H. Contributions of distinct gold species to catalytic reactivity for carbon monoxide oxidation. *Nat. Commun.* **2016**, *7*, 13481. [[CrossRef](#)] [[PubMed](#)]
22. Fu, Q.; Saltsburg, H.; Flytzani-Stephanopoulos, M. Active Nonmetallic Au and Pt Species on Ceria-Based Water-Gas Shift Catalysts. *Science* **2003**, *301*, 935–938. [[CrossRef](#)] [[PubMed](#)]
23. Scott, R.W.J.; Sivadinarayana, C.; Wilson, O.M.; Yan, Z.; Goodman, D.W.; Crooks, R.M. Titania-Supported PdAu Bimetallic Catalysts Prepared from Dendrimer-Encapsulated Nanoparticle Precursors. *J. Am. Chem. Soc.* **2005**, *127*, 1380–1381. [[CrossRef](#)] [[PubMed](#)]
24. Frenkel, A.I.; Machavariani, V.S.; Rubshtein, A.; Rosenberg, Y.; Voronel, A.; Stern, E.A. Local structure of disordered Au-Cu and Au-Ag alloys. *Phys. Rev. B* **2000**, *62*, 9364–9371. [[CrossRef](#)]
25. Eveline, B.; van, B.J.A. Electronic and Geometric Structures of Supported Platinum, Gold, and Platinum-Gold Catalysts. *J. Phys. Chem. C* **2007**, *111*, 9761–9768.
26. Liu, X.; Wang, A.; Zhang, T.; Su, D.-S.; Mou, C.-Y. Au–Cu alloy nanoparticles supported on silica gel as catalyst for CO oxidation: Effects of Au/Cu ratios. *Catal. Today* **2011**, *160*, 103–108. [[CrossRef](#)]
27. He, P.; Wang, X.; Liu, Y.; Liu, X.; Yi, L. Comparison of electrocatalytic activity of carbon-supported Au–M (M = Fe, Co, Ni, Cu and Zn) bimetallic nanoparticles for direct borohydride fuel cells. *Int. J. Hydrog. Energy* **2012**, *37*, 11984–11993. [[CrossRef](#)]
28. Qiao, B.; Wang, A.; Yang, X.; Allard, L.F.; Jiang, Z.; Cui, Y.; Liu, J.; Li, J.; Zhang, T. Single-atom catalysis of CO oxidation using Pt₁/FeO_x. *Nat. Chem.* **2011**, *3*, 634–641. [[CrossRef](#)] [[PubMed](#)]

29. Wei, H.; Liu, X.; Wang, A.; Zhang, L.; Qiao, B.; Yang, X.; Huang, Y.; Miao, S.; Liu, J.; Zhang, T. FeO_x-supported platinum single-atom and pseudo-single-atom catalysts for chemoselective hydrogenation of functionalized nitroarenes. *Nat. Commun.* **2014**, *5*, 5634. [CrossRef] [PubMed]
30. Chen, G.; Zhao, Y.; Fu, G.; Duchesne, P.N.; Gu, L.; Zheng, Y.; Weng, X.; Chen, M.; Zhang, P.; Pao, C.W.; et al. Interfacial effects in iron-nickel hydroxide-platinum nanoparticles enhance catalytic oxidation. *Science* **2014**, *344*, 495–499. [CrossRef] [PubMed]
31. Wang, W.-W.; Du, P.-P.; Zou, S.-H.; He, H.-Y.; Wang, R.-X.; Jin, Z.; Shi, S.; Huang, Y.-Y.; Si, R.; Song, Q.-S.; et al. Highly Dispersed Copper Oxide Clusters as Active Species in Copper-Ceria Catalyst for Preferential Oxidation of Carbon Monoxide. *ACS Catal.* **2015**, *5*, 2088–2099. [CrossRef]
32. Yang, Q.; Fu, X.-P.; Jia, C.-J.; Ma, C.; Wang, X.; Zeng, J.; Si, R.; Zhang, Y.-W.; Yan, C.-H. Structural Determination of Catalytically Active Subnanometer Iron Oxide Clusters. *ACS Catal.* **2016**, *6*, 3072–3082. [CrossRef]
33. Shirakawa, S.; Osaki, M.; Nagai, Y.; Nishimura, Y.F.; Dohmae, K.; Matsumoto, S.; Hirata, H. XAFS study on promoting effect of Au via NiO reduction in Au-Ni bimetallic clusters. *Catal. Today* **2017**, *281*, 429–436. [CrossRef]
34. Chistyakov, A.V.; Zharova, P.A.; Nikolaev, S.A.; Tsodikov, M.V. Direct Au-Ni/Al₂O₃ catalysed cross-condensation of ethanol with isopropanol into pentanol-2. *Catal. Today* **2017**, *279*, 124–132. [CrossRef]
35. Sing, K.S.W.; Everett, D.H.; Haul, R.A.W.; Moscou, L.; Pierotti, R.A.; Rouquerol, J.; Siemieniewska, T. Reporting physisorption data for gas/solid systems with special reference to the determination of surface area and porosity. *Pure Appl. Chem.* **1985**, *57*, 603–619. [CrossRef]
36. Li, S.; Zhang, Y.; Li, X.; Yang, X.; Li, Z.; Wang, R.; Zhu, H. Preferential Oxidation of CO in H₂-Rich Stream Over Au/CeO₂-NiO Catalysts: Effect of the Preparation Method. *Catal. Lett.* **2017**, *148*, 328–340. [CrossRef]
37. Mahammadunnisa, S.; Manoj Kumar Reddy, P.; Lingaiah, N.; Subrahmanyam, C. NiO/Ce_{1-x}Ni_xO_{2-δ} as an alternative to noble metal catalysts for CO oxidation. *Catal. Sci. Technol.* **2013**, *3*, 730–736. [CrossRef]
38. Karpenko, A.; Leppelt, R.; Plzak, V.; Behm, R. The role of cationic Au³⁺ and nonionic Au⁰ species in the low-temperature water-gas shift reaction on Au/CeO₂ catalysts. *J. Catal.* **2007**, *252*, 231–242. [CrossRef]
39. Li, Q.; Zhang, Y.; Chen, G.; Fan, J.; Lan, H.; Yang, Y. Ultra-low-gold loading Au/CeO₂ catalysts for ambient temperature CO oxidation: Effect of preparation conditions on surface composition and activity. *J. Catal.* **2010**, *273*, 167–176. [CrossRef]
40. Wang, D.; Yu, H.; Zhu, Y.; Song, C. NiO nanosheets rooting into Ni-doped CeO₂ microspheres for high performance of CO catalytic oxidation. *Mater. Lett.* **2017**, *198*, 168–171. [CrossRef]
41. Zhang, X.; Li, K.; Shi, W.; Wei, C.; Song, X.; Yang, S.; Sun, Z. Baize-like CeO₂ and NiO/CeO₂ nanorod catalysts prepared by dealloying for CO oxidation. *Nanotechnology* **2017**, *28*, 045602. [CrossRef] [PubMed]
42. Deng, W.; Frenkel, A.I.; Si, R.; Flytzani-Stephanopoulos, M. Reaction-Relevant Gold Structures in the Low Temperature Water-Gas Shift Reaction on Au-CeO₂. *J. Phys. Chem. C* **2008**, *112*, 12834–12840. [CrossRef]
43. Langford, J.I. Powder pattern programs. *J. Appl. Crystallogr.* **1971**, *4*, 259–260. [CrossRef]
44. Langford, J.I. The accuracy of cell dimensions determined by Cohen's method of least squares and the systematic indexing of powder data. *J. Appl. Crystallogr.* **1973**, *6*, 190–196. [CrossRef]
45. Yu, H.-S.; Wei, X.-J.; Li, J.; Gu, S.-Q.; Zhang, S.; Wang, L.H.; Ma, J.-Y.; Li, L.-N.; Gao, Q.; Si, R. The XAFS beamline of SSRF. *Nucl. Sci. Tech.* **2015**, *26*, 050102.
46. Frenkel, A.I.; Wang, Q.; Marinkovic, N.; Chen, J.G.; Barrio, L.; Si, R.; Cámara, A.L.; Estrella, A.M.; Rodriguez, J.A.; Hanson, J.C. Combining X-ray Absorption and X-ray Diffraction Techniques for in Situ Studies of Chemical Transformations in Heterogeneous Catalysis: Advantages and Limitations. *J. Phys. Chem. C* **2011**, *115*, 17884–17890. [CrossRef]

